Chinese Chemical Letters 35 (2024) 109522

Contents lists available at ScienceDirect

Chinese Chemical Letters

journal homepage: www.elsevier.com/locate/cclet

Phthalocyanine self-assembled nanoparticles for type I photodynamic antibacterial therapy

Wei Su[a,*], Xiaoyan Luo[a], Peiyuan Li[b,*], Ying Zhang[b], Chenxiang Lin[a,*], Kang Wang[c], Jianzhuang Jiang[c,*]

[a] Guangxi Key Laboratory of Natural Polymer Chemistry and Physics, Nanning Normal University, Nanning 530000, China
[b] College of Pharmacy, Guangxi University of Chinese Medicine, Nanning 530000, China
[c] Beijing Advanced Innovation Center for Materials Genome Engineering, Beijing Key Laboratory for Science and Application of Functional Molecular and Crystalline Materials, Department of Chemistry and Chemical Engineering, School of Chemistry and Biological Engineering, University of Science and Technology Beijing, Beijing 100083, China

ARTICLE INFO

Article history:
Received 20 November 2023
Revised 6 January 2024
Accepted 11 January 2024
Available online 28 January 2024

Keywords:
Phthalocyanine
Nanoparticles
Photodynamic therapy
Type I reactive oxygen species
Antibacterial therapy

ABSTRACT

Most photodynamic therapies (PDT) rely on reactive oxygen species (ROS) produced by type II mechanisms. However, since the production of type I ROS is not limited by oxygen content, making it more favorable for antimicrobial phototherapy in complex microenvironments. Herein, we report a substituent cationization design strategy that not only improves the hydrophilicity of the prepared phthalocyanine molecule, but also promotes the electron transfer process in the photosensitizer, resulting in the strong type I photodynamic effect of the phthalocyanine self-assembled photosensitizer to efficiently generate $O_2^{\bullet-}$ under both normal and hypoxic conditions. This in combination with its excellent bacteria recognition capability derived from the cationic part on its surface and intrinsic photothermal therapy effect of the phthalocyanine macrocycle endows the phthalocyanine self-assembled photosensitizer with excellent phototherapeutic antimicrobial properties in preclinical models, effectively promoting the wound healing process. This work provides a promising strategy for designing efficient multi-mode photosensitizers.

In recent years, diseases caused by bacterial infections have increased rapidly, seriously endangering human life and safety [1]. Although antibiotics have been revealed to be able to effectively fight bacterial infection, the abuse of antibiotics often leads to the emergence of bacterial resistance [2,3]. Therefore, it is of great significance to develop new antimicrobial treatments [4–6]. Phototherapy particularly photodynamic therapy (PDT) has attracted increasing attention as a promising new antimicrobial therapy [7,8].

The bactericidal mechanism of PDT is caused by reactive oxygen species (ROS) produced after the photosensitizer is irradiated [9]. After illumination, photosensitizers can produce type I ROS by electron transfer, such as hydroxyl radicals ($HO^{\bullet}$) and superoxide radicals ($O_2^{\bullet-}$) [10,11], or type II ROS by energy transfer, such as singlet oxygen ($^1O_2$) [12,13]. While type II ROS needs to be formed in an oxygen-rich environment to play an effective curative effect, type I PDT is less oxygen-dependent and in turn shows better antimicrobial universality in a variety of different physiological microenvironments [14]. Therefore, the design and development of type I PDT photosensitizers have great application potential in antimicrobial therapy.

Phthalocyanine has wide application prospects in the field of phototherapy because of its excellent photochemical properties, strong photostability, and easy chemical modification [15,16]. Among this series of compounds, silicon(IV) phthalocyanine is a promising second-generation photosensitizer, among which Pc4 and RM-1929 have entered clinical trials [17,18]. However, silicon(IV) phthalocyanine usually produces $^1O_2$ by type II mechanisms [19,20], while the production of $O_2^{\bullet-}$ by type I mechanisms has been less reported [21,22]. Moreover, owing to its hydrophobicity and strong π-π interaction, phthalocyanine easily aggregates in water, which affects the occurrence of its photoreaction. To address these issues, Lin *et al.* used metal-organic framework loaded with zinc phthalocyanine photosensitizer to enhance its $^1O_2$ production [23]. Li *et al.* reported that morpholine-containing silicon phthalocyanines exhibited a type I mechanism after assembly with albumin [21]. Duan *et al.* reported that the Schottky junction nanozyme based on Mn-bridged Co-phthalocyanines and $Ti_3C_2T_x$ nanosheets showed type I and II photosensitization [24]. However, the addition of disperse matrix will increase the ineffective

* Corresponding authors.
E-mail addresses: suwmail@163.com (W. Su), lipearpear@163.com (P. Li), cxlinchem@163.com (C. Lin), jianzhuang@ustb.edu.cn (J. Jiang).

https://doi.org/10.1016/j.cclet.2024.109522
1001-8417/

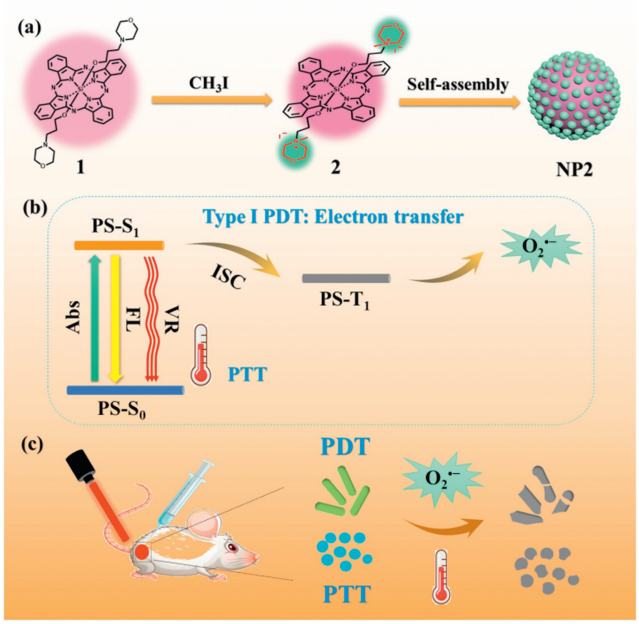

Fig. 1. (a) The structure of **2** and its self-assembly to form NP2. (b) Mechanism of type I PDT and PTT effects. (c) Bacterial infected wound model of mice.

components in the photosensitizer. Li and coworkers modified 2,4,6-tris-(*N*,*N*-dimethylaminomethyl)phenoxy and perphenazine onto phthalocyanine respectively to form amphiphilic structures and then self-assemble into nanoparticles, which demonstrated effective type I PDT [22,25]. This indicates that phthalocyanine can be transformed from type II to type I PDT effect by structural modification. Inspired by these previous research results, we attempt to further modify the physical and chemical properties of silicon(IV) phthalocyanine with morpholine. The N element in morpholine structure can be cationized to form cationic groups, which can enhance its water solubility. At the same time, cationic groups are strong electron acceptors, which facilitate the process of intramolecular charge separation and transfer, resulting in the generation of free radicals by electron transfer between the excited state photosensitioner and the surrounding substrate [26,27].

Here, we designed and synthesized axially substituted bis[3-(*N*-morpholinyl)propoxy]phthalocyaninato silicon (**1**), and then cationized N on the morpholine groups to obtain bis[(3-(*N*-methyl-*N*-morpholinyl)propoxy]phthalocyaninato silicon(IV) diiodide (**2**, Fig. 1a). The cationized 3-(*N*-methyl-*N*-morpholinyl)propoxy substituent makes **2** a typical amphiphilic molecule, which is conducive to its self-assembly into spherical nanoparticles (NP2, Fig. 1a) with a uniform particle size distribution of 15 nm. In particular, the strong electron acceptor nature of the cationic substituents in **2** effectively promotes the charge separation and transfer process of NP2, facilitating the generation of type I ROS and in turn the effective type I PDT effect. This in combination with its excellent bacteria recognition capability derived from the cationic part on its surface and intrinsic photothermal therapy (PTT) effect of the phthalocyanine macrocycle endows NP2 with excellent phototherapeutic antimicrobial properties in preclinical models, effectively promoting the wound healing process (Figs. 1b and c).

Axially substituted morpholine groups of silicon(IV) phthalocyanine (**1**, Fig. S1 in Supporting information) was designed and synthesized, and corresponding cationized derivative (**2**, Fig. S1) was obtained. Their synthesis and characterization (Figs. S2-S4 in Supporting information) are provided in Supporting information. **1** and **2** were self-assembled in water to form nanoparticles NP1 and NP2, respectively (Fig. 2a). It can be seen from the transmission electron microscopy (TEM) images that NP1 is a spherical particle with an uneven size of 100–200 nm, while NP2 is a uniformly dispersed spherical particle with a diameter of about 16 nm. The results of dynamic light scattering (DLS) are also consistent with

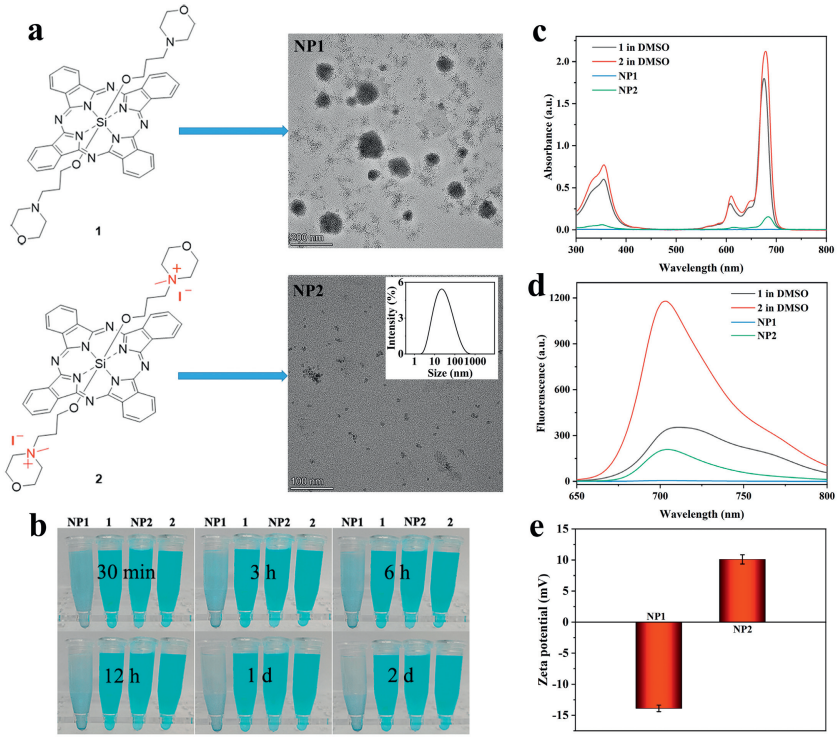

Fig. 2. (a) The preparation process of NP1 and NP2 and their morphology determined by TEM. (b) Images of **1** and **2** in DMSO and NP1 and NP2 (both at 1 μmol/L) in water for different times. (c) Absorption and (d) fluorescence spectra (λ_{ex} = 630 nm) of **1**, **2**, NP1, and NP2 (1 μmol/L) in water and DMSO. (e) Zeta potentials of NP1 and NP2.

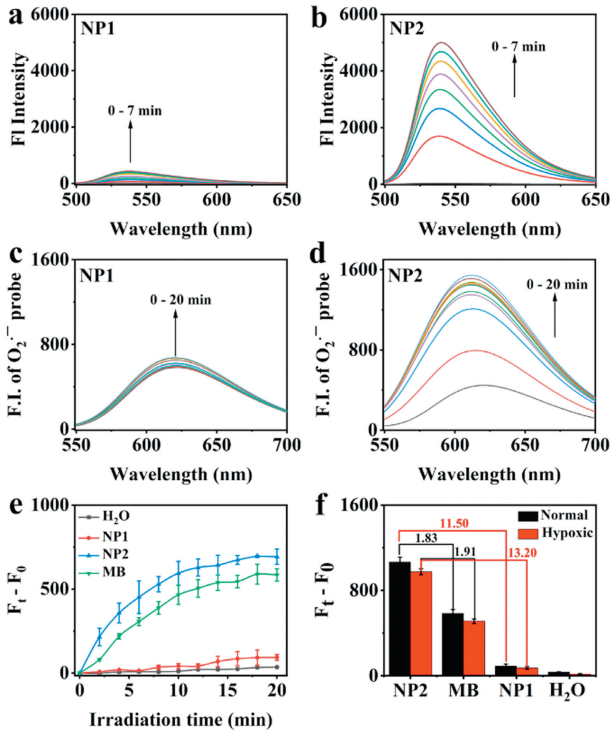

Fig. 3. ROS generation of (a) NP1 and (b) NP2 in water with light irradiation. $O_2^{\bullet-}$ generation of (c) NP1 and (d) NP2 in water with light irradiation. (e) $O_2^{\bullet-}$ generation of NP1, NP2, and MB after irradiation detected by DHE. (f) $O_2^{\bullet-}$ generation of NP1, NP2, and MB upon irradiation (20 min) under normal and hypoxic conditions. All the irradiation is 660 nm, 0.5 W/cm^2. Water as a control. All concentrations were 1 μmol/L.

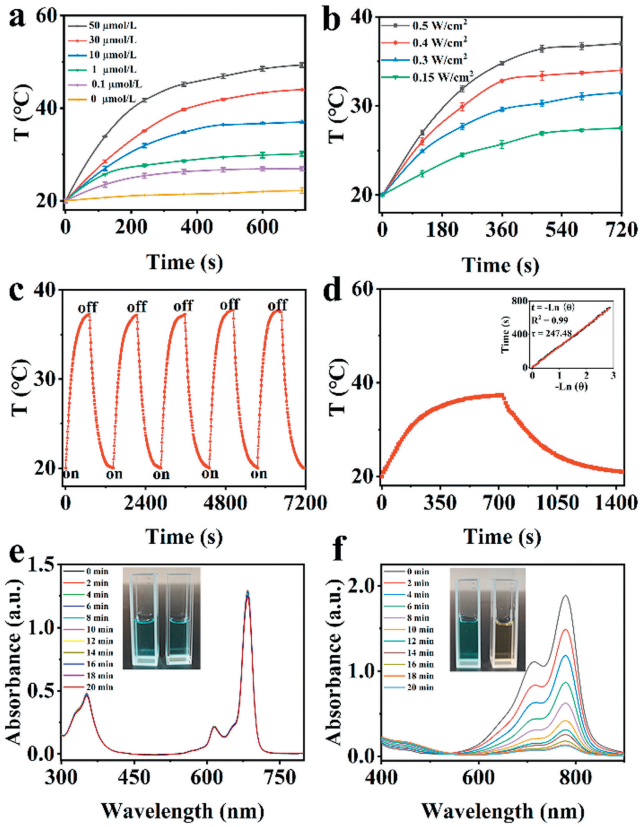

Fig. 4. (a) Temperature measurement of NP2 solutions with different concentrations upon irradiation (0.5 W/cm^2). (b) Temperature measurement of NP2 solution (10 μmol/L) under different power density irradiation. (c) Temperature rise curve of NP2 in 5 ON/OFF cycles. (d) Photothermal effect of NP2 upon irradiation. UV–vis spectra of (e) NP2 and (f) ICG before and after irradiation (0.5 W/cm^2) in H_2O; illustration showing photos before (left) and after (right) irradiation. All the irradiation is 660 nm.

those of SEM images (Fig. 2a). Due to the strong hydrophobicity of **1**, NP1 is unstable and begins to aggregate and precipitate after 3 h (Fig. 2b). After morpholinyl cationization, **2** forms a typical amphiphilic structure, leading to the formation of the stable nano-system NP2. Fig. 2c shows that the UV–vis spectra of **1** and **2** as well as NP1 and NP2. Both **1** and **2** exhibit a sharp Q-band at 680 nm. In contrast, the Q-bands of NP1 and NP2 are significantly reduced. Similarly, the fluorescence of NP1 and NP2 is also significantly quenched with respect to **1** and **2**, which is due to the aggregation of molecules. The fluorescence intensity of NP2 decreased by 5.6-fold compared with that of **2**, thus we may conclude that the charge separation and transfer is more effective in NP2 compared with **2** (Fig. 2d). In addition, fluorescence lifetime was measured with excitation at 365 nm. The longer lifetime of NP2 ($\tau = 4.87$ ns) than that of NP1 ($\tau = 4.46$ ns), demonstrating the better charge-separated state in NP2 (Fig. S5 in Supporting information) [28]. Fig. 2e displays zeta potentials of NP1 and NP2. The potential value of NP2 amount to +10.1 mV, much more positive than that of NP1, −13.9 mV, attributed to the fact that the surface of NP2 nanoparticles is covered with positively charged *N*-methyl-*N*-morpholinyl. This is able to increase the recognition capability of NP2 towards bacterial membranes during the antimicrobial process, enhancing the antimicrobial effect of NP2 [29–31].

Using DCFH as a fluorescent probe, the total ROS generation performance of NP1 and NP2 was investigated [32]. As shown in Fig. 3a, under 660 nm illumination, the fluorescence emission peak of DCFH in NP1 at 535 nm was only slightly enhanced, indicating that only a small amount of ROS was generated. This may be due to the photoelectron transfer effect induced by the lone electron on morpholinyl N of NP1, which inhibits the generation of ROS [26]. The fluorescence of DCFH in NP2 at 535 nm was significantly enhanced with the illumination time, indicating that it can produce abundant ROS (Fig. 3b). Using MB as the reference, it was found that the ROS generation rate after 7 min of illumination was NP2 > MB > NP1, and the ROS generation rate of NP2 was 1.12-fold higher than that of MB (Figs. S6-S8 in Supporting information).

In order to confirm the type of ROS, DHE was used as a probe to evaluate the generation capacity of $O_2^{\bullet-}$ [22]. Compared with NP1, NP2 showed stronger $O_2^{\bullet-}$ generation capacity (Figs. 3c and d), consistent with the results of total ROS. Moreover, the $O_2^{\bullet-}$ generation capacity of NP2 is 1.83-fold higher than that of MB (Fig. 3e, Figs. S9 and S10 in Supporting information). Furthermore, the $O_2^{\bullet-}$ generation capacity of the nanoparticles was tested under hypoxic conditions. As shown in Fig. 3f, under hypoxia conditions, the fluorescence intensity of NP2 did not significantly decrease compared with that in normal condition, and the $O_2^{\bullet-}$ yield of NP2 is 1.91 and 13.20 times higher than those of MB and NP1, respectively. This result reveals that the ability of NP2 to generate $O_2^{\bullet-}$ under light irradiation is independent of O_2 level, indicating excellent type I PDT performance of NP2 under hypoxia environment. This is probably due to the strong electron-withdrawing nature of the cationized morpholinyl group in **2** is able to effectively promote the separation and transfer of charge between cationized morpholinyl group and the phthalocyanine macrocycle in NP2, and thus greatly promote the formation of $O_2^{\bullet-}$ [26,27].

In addition, the photothermal property of NP2 was also studied. As shown in Fig. 4a, the temperature of NP2 rises with the increase of concentration under light irradiation. Among them, the temperature of NP2 solution with a concentration of 50 μmol/L is increased by about 30 °C, and the temperature change was

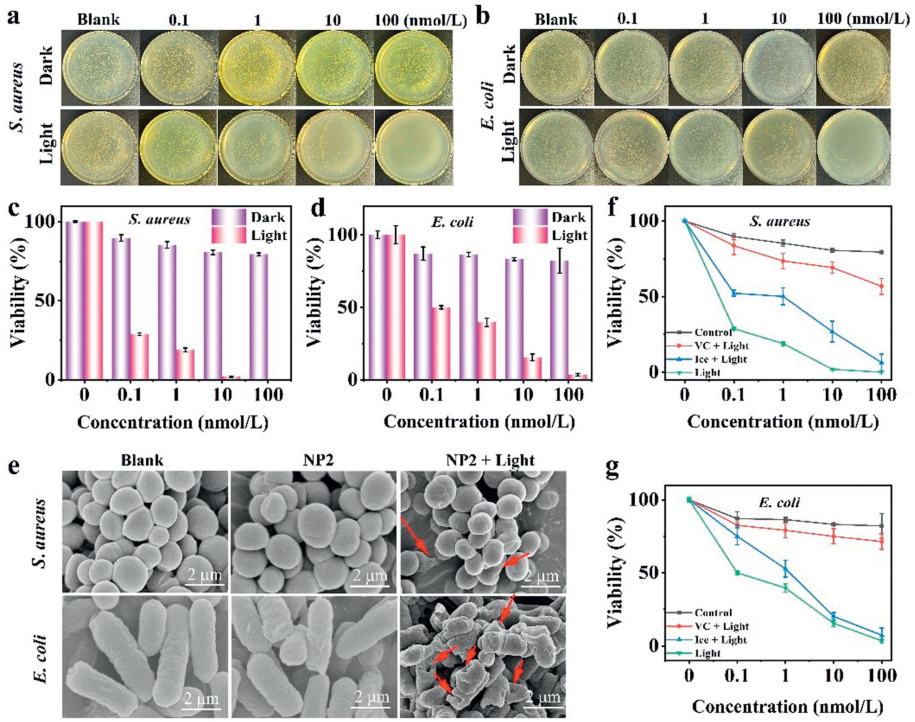

Fig. 5. Photos and viability of (a, c) *S. aureus* and (b, d) *E. coli* treated with NP2. (e) SEM images of *S. aureus* and *E. coli* before and after treated with NP2. PDT (ice + light) and PTT (VC + light) effect of NP2 on (f) *S. aureus* and (g) *E. coli* Error bars indicate mean ± SD ($n \geq 3$).

not obvious when water was used as the control. Fig. 4b shows that the temperature of NP2 rises with the increase of irradiation power under the same concentration, illustrating that the photothermal performance of NP2 is power-dependent. As shown in Fig. 4c, the temperature variation range of NP2 did not change significantly within 5 cycles, demonstrating that NP2 has good photothermal stability. According to the cooling curve (Fig. 4d), it is calculated that the photothermal conversion efficiency (η) of NP2 under 660 nm illumination is 17.3% [33]. Next, the photostability of NP2 was studied by UV–vis spectroscopy compared with ICG. As shown in Figs. 4e and f, upon 660 nm light irradiation, the absorption peak of ICG gradually decreases, and the color of the solution becomes obviously lighter. In addition, NP2 has no obvious change after irradiation, indicating the good photostability of NP2. These results reveal that NP2 has both type I photoreaction and photothermal effects.

The antibacterial effects of NP1 and NP2 on *Staphylococcus aureus* (*S. aureus*) and *Escherichia coli* (*E. coli*) were studied. As shown in Figs. 5a and b, NP2 shows no significant inhibitory activity against the two bacteria in the absence of light. However, the inhibition of NP2 on the two bacteria is obviously concentration-dependent under irradiation. At 100 nmol/L, the inhibition rate of NP2 to *S. aureus* and *E. coli* reaches 100% and 96.5% (Figs. 5c and d), respectively, showing a good antibacterial effect of phototherapy. In contrast, the inhibition rates of NP1 with a concentration of 100 nmol/L on the two bacteria after irradiation are 52.1% and 27.0% (Figs. S11 and S12 in Supporting information), respectively, indicating the inferior phototherapy antibacterial effect of NP1 to NP2.

Moreover, the surface morphology of bacteria before and after NP2 treatment was observed by SEM [34]. As shown in Fig. 5e, *S. aureus* and *E. coli* in the blank group had intact cell membranes and smooth membrane surfaces. After incubation of NP2 with two kinds of bacteria, the surface of the bacterial membrane did not change significantly. After irradiation, the integrity of the cell membrane of *S. aureus* was destroyed and the cytoplasm flowed out. Similarly, after irradiation, the cell membrane of *E. coli* also appeared to be severely wrinkled and perforated, and its rod-like structure was severely damaged. These results suggest that NP2 kills bacteria by destroying their cell membranes under phototoxic effects.

The mechanism of NP2 phototherapy was further investigated. Vitamin C (VC) was used to inhibit the photodynamic antibacterial effect of NP2 (Figs. 5f and g). Compared with NP2 + light group, the antibacterial effect of NP2 + VC + light group was significantly decreased. When the concentration was 100 nmol/L, the inhibition rate of *S. aureus* and *E. coli* was only 43.2% and 28.6%, respectively. Meanwhile, the photothermal antibacterial action of NP2 was inhibited by ice bath (Figs. 5f and g). NP2 + ice + light group still had a stronger antibacterial effect. At the concentration of 100 nmol/L, the antibacterial rate of NP2 + ice + light group against *S. aureus* and *E. coli* were 93.6% and 92.7%, respectively, which was only slightly lower than that of the NP2 + light group. There results indicate that PDT effect of NP2 plays a major role in antimicrobial phototherapy.

The *in vivo* antibacterial action and wound healing ability of NP2 were studied in an animal model infected by *S. aureus* in mice (Fig. 6a), with streptomycin as the control (17.2 mmol/L) and normal saline as the blank [35]. As shown in Figs. 6b and c, the wounds of mice in the blank group were still obviously red and swollen on the 11th day, and the healing rate was only 50.2% (Fig. 6d). The NP2 + light group showed a similar healing ability as the control group. The healing rate of wounds in both groups reached 50% on the 6th day. By the 11th day, the wound redness and swelling subsided in the two groups, and the wound healing rates were 91.6% and 94.5%, respectively (Fig. 6d). Moreover, samples were taken from the wound site during treatment to evaluate the antimicrobial properties of NP2. As shown in Figs. 6e and f, on days 3, 6, and 9, the residual amount of *S. aureus* CFU in the control group and the NP2 + light group was significantly lower than

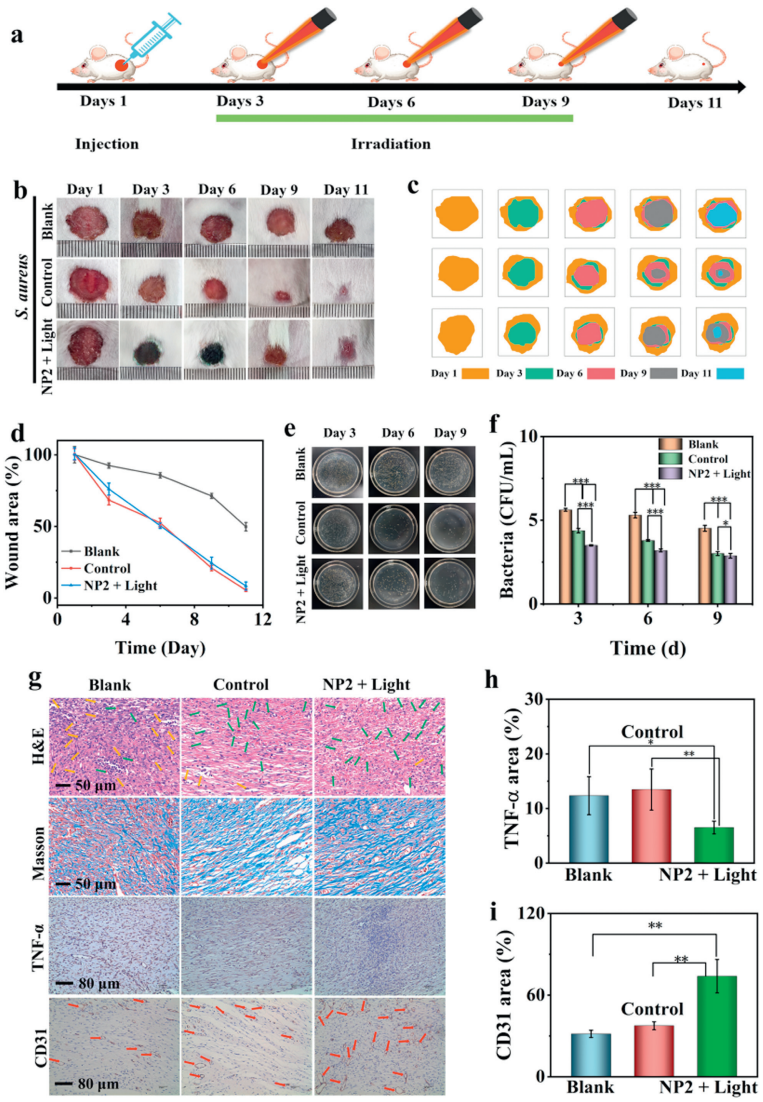

Fig. 6. (a) Schematic diagram of experiments in mice. (b) Photographs and (c) evolution of the wound during treatment. Scale bar = 1 mm. (d) Quantitative analysis of wound areas during treatment. (e) Image and (f) total *S. aureus* CFU (log) on the LB agar plates, $^{*}P < 0.05$, $^{**}P < 0.01$. (g) H&E, Masson, TNF-α and CD31 staining of the wound tissue after 11 days of treatment. Statistics on the relative expression of (h) TNF-α and (i) CD31. Data are presented as mean ± SD ($n = 3$); $^{*}P < 0.05$, $^{**}P < 0.01$.

that in the blank group ($P < 0.05$), indicating that NP2 can effectively promote wound healing through its efficient antibacterial action.

The inflammatory response and angiogenesis of NP2 during wound healing were further investigated by histological analysis of mouse wound sections (Fig. 6g). In the H&E staining, the blank group showed a large number of neutrophils (yellow arrows) and few new vessels (green arrows), indicating a severe inflammatory response. In the Masson staining, the collagen fibers of the control group and NP2 + light group were significantly increased compared with the blank group, indicating faster wound healing in these two groups. In the TNF-α staining, inflammatory factors in the NP2 + light group were significantly reduced compared with the blank group and the control group (Fig. 6h), indicating a mild inflammatory reaction and basically healing of the wound. In CD31 staining, the number of new vessels in NP2 + light was significantly higher than that in the blank group and the control group, indicating that the phototherapy with NP2 resulted in better wound healing (Fig. 6i). The above results provide important evidence that NP2 has excellent phototherapy antimicrobial properties and can effectively promote the healing of infected wounds.

As shown in Fig. 7a, H&E staining analysis of mice organs showed that there were no significant changes in the tissue sections of heart, liver, spleen, lung and kidney in the NP2 + light group compared with the blank and control groups, indicating that NP2 would not cause damage to mouse organs during treatment. Moreover, as shown in Fig. 7b, the body weight of mice in the NP2 + light group was almost the same as that in the control group and the blank group during treatment, which also indicates that NP2 had no effect on the health of mice. Moreover, as shown in Figs. 7c and d, the hemolysis rate of red blood cells treated with NP2 at a concentration of 1000 nmol/L was zero, indicating that it had no hemolytic activity on red blood cells. In addition, the cytotoxicity of NP2 to human embryonic kidney (HEK-293T) cells was detected by CCK-8 assay. As shown in Fig. 7e, cells treated with a higher concentration of NP2 (1000 nmol/L) still maintained a higher viability (≥ 97%), indicating no actual cytotoxicity of NP2 to HEK-293T cells. All these results indicate that NP2 has good biosafety.

In summary, a novel nano-photosensitizer, NP2, was developed by the simple self-assembly of silicon(IV) phthalocyanine axially substituted with cationized morpholinyl. NP2 can produce

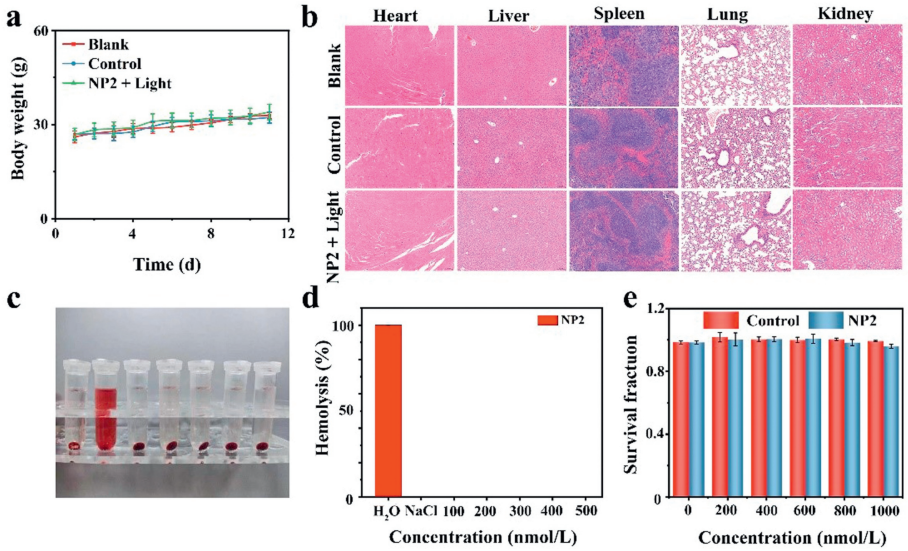

Fig. 7. (a) H&E stained images of major organs of mice ($n = 3$). (b) Body weight curves of mice during treatment. Error bars indicate mean ± SD ($n \geq 8$). (c) Image and (d) hemolysis rate of NP2. Negative control: normal saline; Positive control: water. (e) Cell viability of HEK-293T cells incubated with NP2 for 24 h. Error bars indicate mean ± SD ($n = 3$).

abundant $O_2^{\bullet-}$ through type I mechanism. This in combination with its excellent bacteria recognition capability and intrinsic photothermal therapy effect endows NP2 with excellent phototherapeutic antimicrobial properties. Animal experiments demonstrate the excellent antibacterial and wound healing effect as well as biosafety of NP2 in preclinical models, indicating its great application potential. This work realizes the transformation of phthalocyanine from energy transfer to electron transfer by modifying cationic substituents, which provides a reference strategy for the design of type I photosensitizers.

Declaration of competing interest

The authors declare no competing financial interest.

Acknowledgments

This research was supported by the Central Guidance on the Local Science and Technology Development Fund of Guangxi Province (No. Gui Ke ZY22096010), Guangxi Natural Science Fundation (No. 2023GXNSFAA026181), National Natural Science Foundation of China (No. 51961009), and BAGUI Scholar Program, Guangxi Province, China.

Supplementary materials

Supplementary material associated with this article can be found, in the online version, at doi:10.1016/j.cclet.2024.109522.

References

[1] T.M. Privalsky, A.M. Soohoo, J. Wang, et al., J. Am. Chem. Soc. 143 (2021) 21127–21142.
[2] S. Roy, I. Hasan, B. Guo, Coordin. Chem. Rev. 482 (2023) 215075.
[3] R.T. Mertens, S. Gukathasan, A.S. Arojojoye, C. Olelewe, S.G. Awuah, Chem. Rev. 123 (2023) 6612–6667.
[4] B.T. Liu, X.H. Pan, D.Y. Nie, et al., Adv. Mater. 32 (2020) 2005912.
[5] B.T. Liu, X.H. Pan, D.Y. Zhang, et al., Angew. Chem. Int. Ed. 60 (2021) 25701–539325707.
[6] Q. Yin, P. Zhao, R.J. Sa, et al., Angew. Chem. Int. Ed. 57 (2018) 7691–7696.
[7] X. Hu, H. Zhang, Y. Wang, et al., Chem. Eng. J. 450 (2020) 138129.
[8] X. Cui, Q. Ruan, X. Zhuo, et al., Chem. Rev. 123 (2023) 6891–6952.
[9] D. Wang, H. Wang, L. Ji, et al., ACS Nano 15 (2021) 8694–8705.
[10] G. Yang, J.S. Ni, Y. Li, et al., Angew. Chem. Int. Ed. 60 (2021) 5386–5393.
[11] J. Gong, L. Liu, C. Li, et al., Chem. Sci. 14 (2023) 4863–4871.
[12] E. Pang, S. Zhao, B. Wang, et al., Coordin. Chem. Rev. 472 (2022) 214780.
[13] C. Bloyet, F. Sciortino, Y. Matsushita, et al., J. Am. Chem. Soc. 144 (2022) 10830–10843.
[14] K.X. Teng, L.Y. Niu, Q.Z. Yang, Chem. Sci. 13 (2022) 5951–5956.
[15] P.C. Lo, M.S. Rodríguez-Morgade, R.K. Pandey, et al., Chem. Soc. Rev. 49 (2022) 1041–1056.
[16] B.D. Zheng, Q.X. He, X. Li, J. Yoon, J.D. Huang, Coordin. Chem. Rev. 426 (2021) 213548.
[17] X. Li, B.D. Zheng, X.H. Peng, et al., Coordin. Chem. Rev. 379 (2019) 147–160.
[18] J.M. Johnson, D.M. Cognetti, J.M. Curry, F.E. Mott, et al., Ann. Oncol. 30 (2019) 426.
[19] N. Nwahara, G. Abrahams, J. Mack, E. Prinsloo, T. Nyokong, J. Inorg. Biochem. 239 (2023) 112078.
[20] L. Xu, T. Zhang, B. Huang, et al., Front. Pharmacol. 14 (2023) 1168393.
[21] R. Wang, K.H. Kim, J. Yoo, et al., ACS Nano 16 (2022) 3045–3058.
[22] Y.Y. Zhao, L. Zhang, Z. Chen, et al., J. Am. Chem. Soc. 143 (2021) 13980–13989.
[23] T. Luo, G.T. Nash, Z. Xu, et al., J. Am. Chem. Soc. 143 (2021) 13519–13524.
[24] F. Duan, Q. Jia, G. Liang, et al., ACS Nano 17 (2023) 11290–11308.
[25] X. Li, D. Lee, J.D. Huang, J. Yoon, Angew. Chem. Int. Ed. 57 (2018) 9885–9890.
[26] S. Liu, B. Wang, Y. Yu, et al., ACS Nano 16 (2022) 9130–9141.
[27] Q. Wan, R. Zhang, Z. Zhuang, et al., Adv. Funct. Mater. 30 (2020) 2002057.
[28] L. Zhang, Q.C. Yang, S. Wang, et al., Adv. Mater. 34 (2022) 2108174.
[29] P.P. Kalelkar, M. Riddick, A.J. García, Nat. Rev. Mater. 7 (2022) 39–54.
[30] Y. Wang, E.Y. Chi, D.O. Natvig, K.S. Schanze, D.G. Whitten, ACS Appl. Mater. Interfaces 5 (2013) 4555–4561.
[31] J. Sun, M. Li, M. Lin, B. Zhang, X. Chen, Adv. Mater. 33 (2021) 2104402.
[32] F. Nan, Q. Jia, X. Xue, et al., Biomaterials 284 (2022) 121495.
[33] R. Wang, D. Kim, M. Yang, X. Li, J. Yoon, ACS Appl. Mater. Interfaces 14 (2022) 7609–7616.
[34] W. Su, X. Jiang, Y. Zhang, et al., J. Colloid Interf. Sci. 647 (2023) 201–210.
[35] R. Su, P. Li, Y. Zhang, et al., Carbohyd. Polym. 302 (2023) 120349.